J Water Environ Nanotechnol 2026, 11(SI): 113-128
10.22090/jwent.2025.2070247.1962

RESEARCH PAPER

Effect of Zinc Doping on Structural, Optical, Magnetic, Photocatalytic, and Anti-Microbial Properties of ZrO_2 Nanoparticles Via Machine Learning-Based SEM Image Analysis

Jeba Rengaswamy*[1], Radhika Sathasivam[2], Ascar Davix Xavier Durai[3]

[1]Department of Physics, Women's Christian College, Nagercoil, Tamilnadu, India - 629001.
[2]Department of Physics, Pioneer Kumaraswamy College, Nagercoil,Tamilnadu, India–629003.
[3]Department of Electronics and Communication Engineering, R.V.R. & J.C. College of Engineering, Guntur, Andhra Pradesh, India – 522019

* Corresponding Author. Email: jeba170787@gmail.com

Article History:
Received: 2025-08-25
Revised: 2025-12-15
Accepted: 2025-12-16

How to cite this article
Rengaswamy J, Radhika S, Durai A D X. Effect of Zinc Doping on Structural, Optical, Magnetic, Photocatalytic, and Anti-Microbial Properties of Zro2 Nanoparticles via Machine Learning-Based SEM Image Analysis. J Water Environ Nanotechnol 2026, 11(SI): 113-128, DOI: 10.22090/jwent.2025.2070247.1962

HIGHLIGHTS

- Zn^{2+} doping reduces the bandgap, significantly enhancing photocatalytic degradation efficiency.
- A YOLOv8–ConvNeXt pipeline enables quantitative analysis of particle morphology, agglomeration, and surface topography from SEM images.
- Zn^{2+} doped ZrO_2 exhibits significant antibacterial (23 mm) and antifungal (20 mm) inhibition zones, promising for biomedical applications.

ABSTRACT

Pure and zinc-doped zirconium oxide nanoparticles were synthesized using a co-precipitation process, and the effect of zinc doping on their photocatalytic and antimicrobial activities was investigated. The analyte contains Zn^{2+} incorporated into the ZrO_2 matrix at a concentration of x mol%. $Zr_{1-x}Zn_xO_2$ nanoparticles with nominal composition of x = 0.04, 0.08, 0.12 wt. % were synthesized. The co-precipitation technique is based on the simultaneous precipitation of metal ions from an aqueous solution when a precipitating agent increases the pH above the solubility limit of the metal hydroxides. The prepared samples are pure tetragonal phase, as shown by the X-ray diffraction pattern, and the crystallite size increases with an increase in dopant concentration. A machine learning algorithm is introduced for the analysis of SEM images. This algorithm automates SEM image analysis using YOLOv8 and ConvNeXt to quantify nanoparticle morphology, agglomeration, and surface topography, enabling high-throughput, reproducible materials characterization for advanced research applications. The shape of high-dopant Zn demonstrates that it is composed of nanocubes. All samples have magnetic hysteresis loops with diamagnetic background effects, according to VSM tests. When exposed to visible light, increasing the Zn^{2+} doping causes a drop in luminescence intensity. Photocatalytic activity steadily reduced with increasing zinc levels. This might be because excess zinc acts as a recombination center and covers the active sites on the zirconium oxide surface, lowering the effectiveness of charge separation. Zn-doped ZrO_2 has better anti-bacterial and anti-fungal activities.

KEYWORDS

Co-precipitation, YOLOv8,ConvNeXt,Machine Learning, Zn doped ZrO2, photocatalysis, anti-microbial.

©2026 The Author(s). Published by the Iranian Environmental Mutagen Society. This work is licensed under the Creative Commons Attribution 4.0 International License (CC BY 4.0). To view a copy of this license, visit http://creativecommons.org/licenses/by/4.0/.

1 INTRODUCTION

Zirconia nanoparticles (ZrO_2 NPs) are versatile nanomaterials with significant applications as adsorbents, nanosensors, and nanocatalysts. Their notable biological properties—including antimicrobial, antioxidant, and anti-cancer activity—have further spurred interest in their use for biomedical applications, such as drug delivery systems and advanced dental therapeutics. The growing prominence of ZrO_2 NPs has necessitated a thorough investigation of their various synthetic methodologies [18]. Doping zirconia (ZrO_2) is critically important because it stabilizes its crystal structure, preventing a destructive phase change that causes pure ZrO_2 to crack[1]. By adding dopants, zirconia gains exceptional fracture toughness through a process called transformation toughening, where volume expansion around cracks stops their propagation. This enhances mechanical strength, wear resistance, and thermal properties. Doping also introduces oxygen ion conductivity, vital for solid oxide fuel cells and sensors. These improvements make doped zirconia essential for advanced applications in biomedicine, cutting tools, thermal coatings, and energy technologies.

Zinc, particularly as zinc oxide (ZnO), plays a critical role in photocatalysis due to its ability to efficiently generate electron-hole pairs under UV light to degrade organic pollutants and facilitate water splitting. Its antimicrobial significance stems from the release of Zn^{2+} ions, which disrupt microbial cell membranes and generate reactive oxygen species, leading to cell death. This dual functionality makes zinc-based materials highly valuable for environmental remediation, such as purifying wastewater, and for creating self-disinfecting surfaces in medical and hygienic applications, promoting public health and sustainability.

In the synthesis approaches, such as co-precipitation, water and hydroxyl ions have a strong affinity to ferric ions in the hydrolysis of ions under a proper molar ratio [23]. The fundamental importance of co-precipitation is its ability to mix multiple chemical elements at the atomic level in a liquid solution and then precipitate them out together as a solid compound. This ensures a high degree of chemical homogeneity (uniform distribution of elements) in the resulting powder, which is critical for the performance of many advanced materials.

Machine Learning (ML) is a subset of artificial intelligence (AI) where computer systems learn patterns from data without being explicitly programmed for specific tasks. Instead of following rigid instructions, ML algorithms identify statistical patterns in data to make predictions, classifications, or decisions. Scanning Electron Microscopy (SEM) produces high-resolution images of nanomaterials, but manual analysis is slow, subjective, and impractical for large datasets. ML automates and enhances this analysis.

A key application is automated nanoparticle detection and segmentation, where algorithms like YOLO or Mask R-CNN precisely identify and outline individual particles, enabling rapid analysis of thousands of nanoparticles in minutes—a task that would take researchers hours manually. This is closely followed by detailed morphological characterization, where ML algorithms calculate essential shape descriptors such as particle size distribution, circularity, aspect ratio, and solidity, providing statistical insights into material properties. Additionally, ML excels in agglomeration analysis, employing clustering algorithms like DBSCAN to quantify particle dispersion, measure inter-particle distances, and classify agglomerates, which is crucial for understanding material behavior in applications like catalysis or composites.

Doping zirconia (ZrO_2) with zinc (Zn) imparts significant functional advantages, primarily enhancing its photocatalytic and biomedical efficacy. Zn incorporation reduces ZrO_2's band gap, enabling efficient visible-light absorption and boosting its ability to degrade organic pollutants under solar radiation. Additionally, Zn-doped ZrO_2 exhibits strong antimicrobial properties, as released Zn^{2+} ions disrupt microbial membranes and generate oxidative stress. This dual functionality makes it valuable for environmental applications like wastewater treatment and for creating self-sterilizing surfaces in medical devices, overcoming the limitations of pure ZrO_2.

The manufacture of Zirconium Oxide nanoparticles is done in a variety of ways. The Co-precipitation method is employed to prepare Zn-doped Zirconia nanoparticles in this paper. For the creation of nanoparticles, the co-precipitation approach is straightforward and effective [2-5].

Zn-doped ZrO_2 is commonly synthesized using methods such as sol-gel, co-precipitation, and hydrothermal synthesis. For instance, [19] used a sol-gel method to incorporate Zn into the ZrO_2 lattice, observing a transition from monoclinic to tetragonal phase stability at room temperature with increasing Zn concentration. Study [20] demonstrates additive manufacturing of 3D zinc-doped zirconia microarchitectures via two-photon lithography. Zn doping modifies crystallinity and optical properties, stabilizing monoclinic ZrO_2 at lower temperatures and enhancing high-energy photon emission due to oxygen vacancies. Although Zn forms transient ZnO phases that sublimate, the work reveals how defects tune optical functionality in ZrO_2, enabling advanced tailored ceramics for photonic applications through controlled doping and annealing processes.

The practical application of these photocatalysts has been hampered by several limitations, including the need for photocatalyst optimization to improve quantum yield and the inability to absorb light in the visible region. The latter issue can be addressed by doping metals or anion impurities into nanosized metal oxides, employing dye sensitizers, or combining nanosized oxides with narrow band-gap semiconductors to form hybrid nanoparticles or nanocomposites [6]. Few studies

J Water Environ Nanotechnol, 2026, 11(SI): 113-128
10.22090/jwent.2025.2070247.1962

were found for the zinc-doped ZrO_2 nanoparticles. The effect of Zinc doping on structural, optical, magnetic, photocatalytic, and antimicrobial properties of Zirconium oxide nanoparticles was presented in this paper. The major contributions of the proposed method are as follows,

- Zn-doped Zirconia nanoparticles were synthesized using the Co-Precipitation technique. The doping of Zn^{2+} has shown better photocatalytic degradation efficiency due to the reduction of the bandgap.
- The proposed algorithm provides a comprehensive pipeline for quantitatively analyzing particle morphology, agglomeration state, and surface topography from scanning electron microscopy (SEM) images by integrating instance segmentation capabilities of YOLOv8 with the advanced texture classification power of ConvNeXt.
- The anti-microbial properties of Zn^{2+} doped ZrO_2 were studied. The obtained results revealed that the inhibition zone of 23mm for Staph aureus as an anti-bacterial agent and 20mm for Candida albicans as an anti-fungal agent signifying their prospective use as implant coatings, wound dressings, etc.

2. EXPERIMENTAL TECHNIQUE

2.1 Pure and Zn-Doped ZrO_2 Nanoparticles by Co-precipitation Method

For the synthesis of $Zr_{1-x}Zn_xO_2$ nanoparticles with nominal composition x = 0.04, 0.08, 0.12 wt. %. A calculated amount of Zinc Chloride solution was used. NaOH as a precipitating agent, pure and Zn-doped zirconium oxide nanoparticles were synthesized. The ratio of Zirconium oxychloride to sodium hydroxide in an aqueous solution was 0.5:2. Drops of NaOH solution were added until the pH reached 12, and the mixture was agitated repeatedly for 2 hours at 60°C. Finally, to remove contaminants, the resulting precipitate slurry was filtered and washed with distilled water several times before being rinsed with acetone. After drying, the residue was crushed into a fine powder using a mortar and pestle. The resulting ZrO_2 was then annealed for 2 hours at 500°C. Following that, Zn-doped ZrO_2 nanoparticles for 0.04, 0.08, and 0.12 wt% Zinc concentrations were synthesized using the same process; the resulting products are referred to as Zn-1, Zn-2, and Zn-3, respectively.

2.2 Photocatalytic activity test

The photocatalysis process is extensively studied for eliminating diverse contaminants from water and wastewater. Zirconium dioxide (ZrO_2), a widely used metal oxide semiconductor, offers advantageous characteristics such as non-toxicity, strong stability under both acidic and alkaline conditions, and high thermal resistance. Its favorable conduction and valence band energy levels further enhance its suitability. Consequently, ZrO_2 presents considerable promise as an effective photocatalyst for degrading pollutants in water treatment applications [25].

On the degradation of methylene blue (MB), the photocatalytic activity of pure and Zn-doped ZrO_2 was investigated. A 0.1M, 50ml aqueous solution of methylene blue was prepared, and 0.2g of photocatalyst (Zn-1, Zn-2, and Zn-3) was suspended in it. The experiment was carried out in the presence of UV light. The photocatalytic experiments were carried out using a 50 W UV halogen lamp, which provides a broad UV–Vis emission with a strong intensity in the UVA region (320–400 nm). The lamp delivers continuous and stable irradiation with sufficient photon flux to activate both pure and Zn-doped ZrO_2 nanoparticles. Its high-power output ensures effective excitation of the photocatalyst, while the constant illumination mode supports consistent dye degradation throughout the reaction. Every 60 minutes, 4ml of dye solution was removed from the system, and the dye removal efficiency was determined using a UV-Vis spectrometer. Further, the degradation efficiency is strongly influenced by electrostatic interactions between the adsorbate and the catalyst surface. These interactions are governed by solution pH, which affects both the surface charge (zeta potential) of the catalyst and the ionization state of the adsorbate, as defined by its pKa. Optimizing the pH to favor opposite charges can therefore enhance initial adsorption and improve overall process performance.

2.3. Kirby-Bauer test (KB test)

The KB test, also known as the disc-diffusion antibiotic sensitivity test, is used for the bacterial inhibition experiment. For the development of bacteria, nutrient agar media with a pH of 7.2 were created and inoculated with the experimental organism. The complete area of antibiotic discs was sprayed with a suspension of gram-positive and gram-negative bacteria. The reference antibiotic is amikacin, which is also spread alongside the disc. The plate was then incubated for 16 hours at 35°C [7]. S. aureus and E. coli were selected as model organisms for antibacterial research due to their clinical importance and their contrasting cell wall structures [24]. In and around the sample, bacterial inhibition zones formed. The diameter of the inhibitory zones was measured after incubation. The agar diffusion method tested the antifungal activity of synthesized materials against Candida Albicans and Candida parapsilosis fungal strains. Nystatin was employed as a reference antifungal. The zone of inhibition is the area where bacterial growth is stopped due to the compound's bacteriostatic activity, and it is used to assess the compound's inhibitory impact on a specific microorganism [8].

2.4 Characterization

The structural properties of synthesized nano zirconia, such as crystallite size and phase identification, were validated

using an XPERT-PRO diffractometer in the 10 ° to 80 ° diffraction angle 2 range. Using a Perkin Elmer Lambda 35 spectrophotometer, UV VIS spectrums for nano ZrO_2 were acquired in the wavelength range of 100 to 1100nm. Scanning electron microscope (SEM) and Energy Dispersed X-Ray (EDX) with EV018(CARL ZEISS) and Quantax 200 with X Flash 6130 were used to observe the structural morphology and chemical condition [9]. The magnetic characteristics of the produced nanoparticles are studied using Lakeshore Vibrating Sample Magnetometer (VSM) measurements.

3 RESULTS AND DISCUSSION

3.1 XRD Analysis

Figure 1 shows the diffraction pattern of pure and zinc-doped zirconium oxide nanoparticles. From Figure 1 (a), the peaks corresponding to the tetragonal phase are 2θ ~ 30.24º, 34.97º, 35.31º, 50.59º, 59.92º,63.04º,74.34º, corresponding to planes (011), (002), (110), (112), (013), (202), (220), respectively are in good agreement with JCPDS card No.50-1089. Except for the ZrO_2 crystalline phase, there were no other XRD diffraction peaks among the four samples (ZrO_2, Zn-1, Zn-2, Zn-3).

This indicates that the Zn ion was well distributed in the host of the ZrO_2 matrix. The outcome shows that the product has a highly crystalline nature. It is identified that there is a slight peak shifting towards lower 2θ values, and the shift is increasing with increasing Zinc content, as seen in Figure 1 (b). This is because of the difference in ionic radius of Zn^{2+} (0.88 Å) compared to Zr^{4+}(0.80 Å), thus Zn ions occupy substitutional and interstitial lattice sites. The crystallite size (D), dislocation density (δ), Stacking Fault (SF), and micro strain (å) were calculated using equations 1, 2, 3, and 4, respectively.

$$D = \frac{0.9\lambda}{\beta \cos\theta} \tag{1}$$

where 'λ' is the wavelength of the X-rays; 'θ' is the Bragg's diffraction angle, and 'β' is the full width at half maximum (FWHM) of the diffraction peaks (in radians).

$$\delta = \frac{1}{D^2} \tag{2}$$

$$SF = \frac{2\pi^2}{45\sqrt{3}\tan\theta} \tag{3}$$

$$\text{å} = \frac{\beta \cos\theta}{4} \tag{4}$$

where β is the FWHM and θ is the diffraction angle.

The lattice parameters and the volume of the unit cell are calculated using equations 5 and 6, respectively [26].

$$\frac{1}{d2} = \frac{h2+k2}{a2} + \frac{l2}{c2} \tag{5}$$

$$V = \frac{\sqrt{3}a^2c}{2} \tag{6}$$

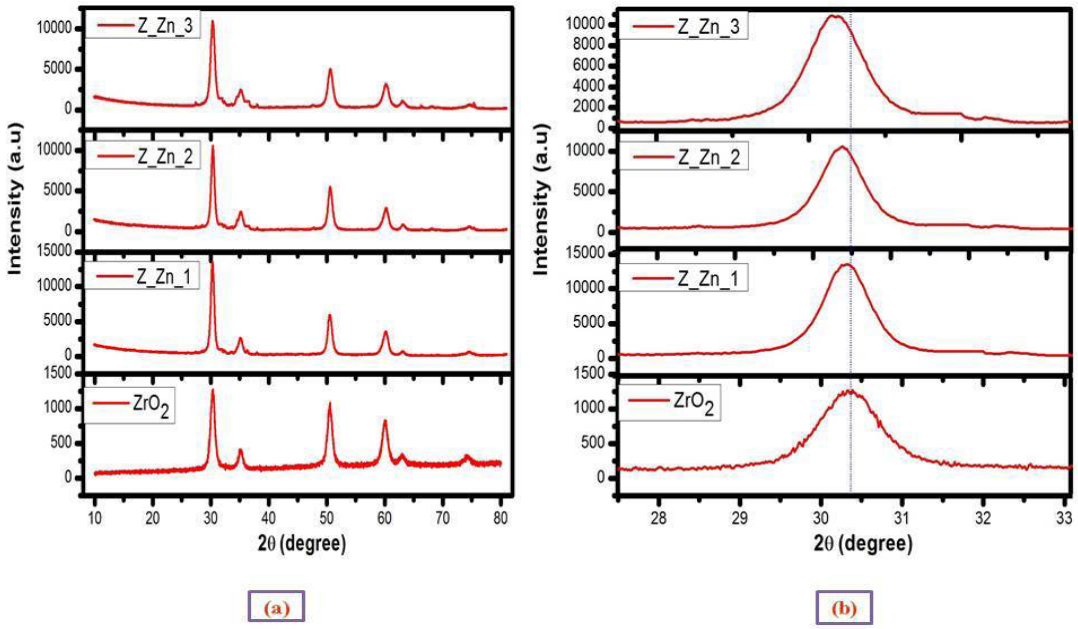


Figure 1. XRD pattern of synthesized pure and Zn- doped ZrO_2 nanoparticles

J Water Environ Nanotechnol, 2026, 11(SI): 113-128
10.22090/jwent.2025.2070247.1962

Table 1. Lattice and geometrical parameters of synthesized pure and Zn-doped ZrO_2 nanoparticles

Sample detail	Lattice parameters				Geometrical parameters			
	a=b (Å)	C (Å)	Aspect ratio 'c/a'	Unit cell volume 'V' $(Å)^3$	Crystallite Size, D (nm)	Micro strain 'ε' (×10−3)	Dislocation density'δ' ($\times10^{15}$ n/m2)	Stacking fault
Pure	3.59	5.27	1.47	58.82	29.74	1.26	1.23	0.48
Zn-1	3.604	5.13	1.42	57.57	11.40	2.83	7.69	0.49
Zn-2	3.61	5.07	1.40	57.22	11.87	2.82	7.1	0.49
Zn-3	3.60	5.11	1.41	57.35	11.91	1.74	7.05	0.49

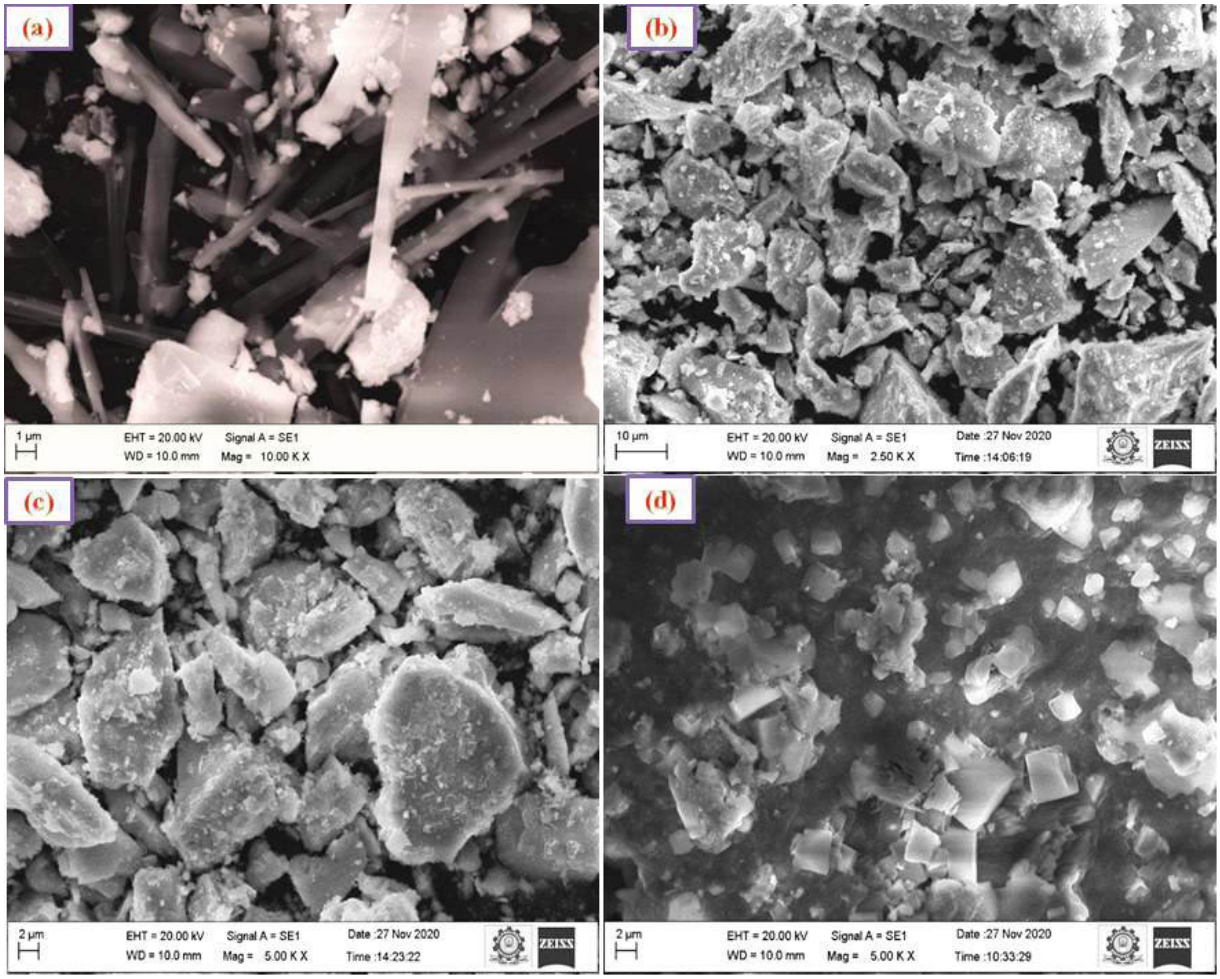


Figure 2. SEM images of synthesized pure and Zn-doped ZrO2 nanoparticles

It shows that crystallite size increases with increasing dopant concentration. Internal strain is produced in the parent ZrO_2 system due to a mismatch in the ionic radii of 'Zn' and 'Zr'. Table 1 shows that the strain in ZrO_2 nanocrystals decreases as the 'Zn' concentration increases. Atoms stuck in non-equilibrium positions are easily moved to more equilibrium positions when Zn^{+2} ions are absorbed into the host ZrO_2 lattice. The moving of atoms might release the strain [10]. As seen in Table 1, the decrease in strain generated an increase in the crystallite size of nanoparticles.

3.2 SEM and EDX Analysis

The morphology of zinc-doped ZrO_2 nanoparticles is investigated by scanning electron microscope (SEM). The micrographs of undoped and zinc-doped ZrO_2 nanoparticles under various concentrations are shown in Figure 2 (a-d).

A fully automated image processing technique was used for the analysis of physical properties and deposition of asphaltenes on the surfaces. A decision-making algorithm for Denoising and Mask Generation was used [21]. Various machine learning concepts, such as Principal Component Analysis (PCA), Linear Regression (LR), and Gaussian Process Regression (GPR), were used for the investigation of SEM images of SiOx materials [22]. This study compares the cross-sections from different samples.

The integration of machine learning (ML) with scanning electron microscopy (SEM) image analysis represents a transformative advancement in nanomaterials characterization. Traditional methods for quantifying particle size, shape, agglomeration, and surface topography are often time-consuming and subjective. Supervised ML algorithms, particularly convolutional neural networks (CNNs) like Mask R-CNN, enable automated, high-throughput, and precise extraction of these morphological features. By training models on annotated SEM datasets, this approach ensures reproducible, bias-free analysis, unlocking deeper insights into structure-property relationships in materials such as Zn-doped ZrO_2 nanoparticles and accelerating research and development in materials science and engineering.

The proposed algorithm provides a comprehensive pipeline for quantitatively analyzing particle morphology, agglomeration state, and surface topography from scanning electron microscopy (SEM) images by integrating instance segmentation capabilities of YOLOv8 with the advanced texture classification power of ConvNeXt. The method enables high-throughput, reproducible characterization of nanomaterials. The proposed algorithm is briefed in this section.

Algorithm:

Step 1: Image Preprocessing and Calibration

1.1 Scale calibration:

· Extract scale bar information from image metadata or manual annotation

· Calculate pixels-to-microns conversion factor: γ = (physical length)/(pixel length)

· Store calibration factor for all subsequent measurements

1.2 Image normalization:

· Apply contrast-limited adaptive histogram equalization (CLAHE) to enhance features

· Normalize pixel intensities to [0, 1] range: I_norm = (I - min(I))/(max(I) - min(I))

· Resize image to YOLOv8-compatible dimensions (640 × 640) while maintaining aspect ratio with padding

1.3 Patch extraction for texture analysis:

· Divide original image into overlapping 224 × 224 patches P_j with stride 112

· Store spatial coordinates for each patch for reconstruction

Step 2: Instance Segmentation Using YOLOv8-Seg

2.1 Model initialization:

· Load pre-trained YOLOv8-seg model

· Configure confidence threshold (0.7) and IoU threshold (0.6)

2.2 Inference and segmentation:

· Process the normalized image through YOLOv8 to obtain:

o Bounding boxes B_i = [x_min, y_min, x_max, y_max, confidence]

o Instance segmentation masks M_i for each detected particle

o Class predictions C_i (if multiple particle types present)

2.3 Post-processing:

· Apply non-maximum suppression to eliminate overlapping detections

· Filter masks using confidence thresholding

· Convert mask coordinates to original image dimensions using inverse transformation

Step 3: Shape Analysis from Segmentation Masks

3.1 Morphological processing:

· Apply binary closing to fill small holes in masks: $M_i' = M_i \bullet K$, where K is 3×3 structuring element

· Smooth mask boundaries using morphological opening

3.2 Shape descriptor extraction for each mask M_i:

· Area: $A_i = \gamma^2 \times \Sigma$ pixels in M_i

· Perimeter: $P_i = \gamma \times$ chain code length of mask boundary

· Circularity: $C_i = (4\pi A_i)/(P_i)^2$

· Aspect ratio: AR_i = (Major axis length)/(Minor axis length)

· Solidity: S_i = A_i / Area of convex hull

· Roundness: $R_i = (4A_i)/(\pi \times (\text{Major axis})^2)$

3.3 Particle classification by shape:

· Implement rule-based classification:

o Spherical: $C_i > 0.9$, $AR_i < 1.2$

o Rod-like: $AR_i > 3.0$

o Cubes : $AR_i = 0.5$

J Water Environ Nanotechnol, 2026, 11(SI): 113-128
10.22090/jwent.2025.2070247.1962

o Irregular: C_i < 0.7

Step 4: Agglomeration Analysis

4.1 Spatial clustering:

· Extract centroid coordinates for all detected particles: C_i = [x_i, y_i]

· Apply DBSCAN clustering with parameters ε = 10 pixels and min_samples = 3

· Identify cluster labels L_i for each particle

4.2 Agglomeration metrics:

· Agglomeration degree: AD_k = N_k / A_k for each cluster k

· Primary particle ratio: PPR = (Number of single particles)/(Total particles)

· Cluster size distribution: Histogram of particles per cluster

· Inter-particle distance: Mean nearest-neighbor distance within clusters

4.3 Aggregate morphology:

· For each cluster, calculate:

o Convex hull area

o Fractal dimension using the box-counting method

o Compactness: (Area of cluster)/(Area of convex hull)

Step 5: Surface Topography Analysis Using ConvNeXt

5.1 Texture model initialization:

· Load pre-trained ConvNeXt-Base model

· Replace classifier head with custom head for texture classes (smooth, porous, rough, cracked)

· Load fine-tuned weights for SEM texture analysis.

5.2 Patch-based texture classification:

· For each patch P_j:

o Normalize using ImageNet statistics

o Obtain texture class probabilities: T_j = ConvNeXt(P_j)

o Assign dominant class: C_j = argmax(T_j)

· Reconstruct the texture probability map for the entire image

5.3 Topography quantification:

· Texture distribution: Percentage coverage of each texture class

· Spatial heterogeneity: Entropy of texture class distribution

· Feature size: Auto-correlation length for each texture class

· Surface roughness: Statistical analysis of intensity variations within texture classes

The pure ZrO_2 consists of finer, highly rod-shaped nanoparticles that exhibit an extremely strong tendency to form large, dense, and continuous agglomerates. The surface topography is exceptionally complex and porous. The reduced

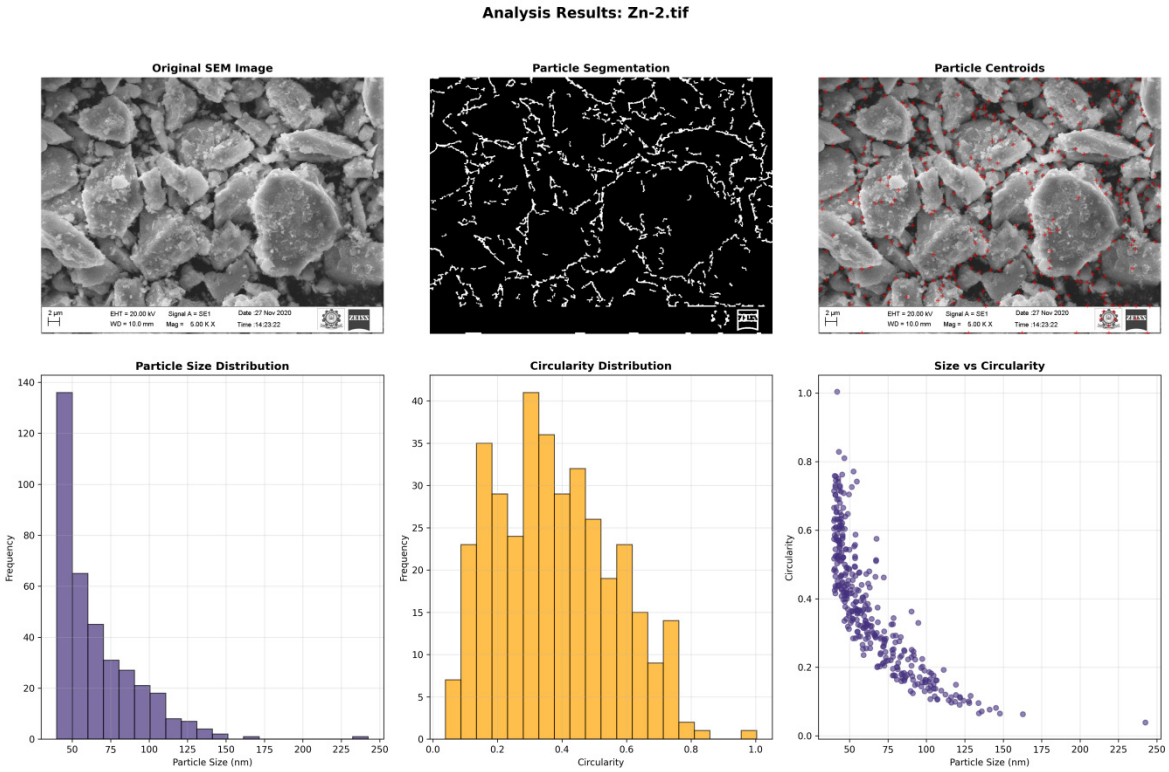


Figure 3. SEM image Analysis of the synthesized sample Zn-2

inter-particle distance suggests potential sintering or very strong cohesive forces. This morphology is typical for high-surface-area nanomaterials used in applications like catalysis, where maximized active sites are critical, but also presents challenges for dispersion.

The low-magnification view reveals the flake-like structure of the sample Zn-1, dominated by large, irregular agglomerates (2.5 ± 1.5 μm) that form a highly connected network covering ~85% of the surface. The structure contains significant porosity (~15%) between agglomerates. This morphology suggests a cohesive powder with strong inter-particle forces that form large aggregates. The structure would likely influence bulk properties like flowability, packing density, and dissolution behavior, making this information crucial for understanding the material's performance in applications like powder metallurgy or pharmaceutical formulations.

The sample Zn-2 consists of polydisperse, predominantly spherical ZrO_2 nanoparticles with a strong tendency to form large, dense agglomerates. The surface topography is highly complex and primarily rough/porous, which is consistent with the aggregated nanoparticle morphology. This suggests a high surface area and potential application in catalysis or sensing.

Zn doping significantly alters the morphology of ZrO_2. Compared to undoped ZrO_2 at the same magnification, the Zn-3 sample exhibits a decrease in mean particle size, more irregular particle shapes, a higher proportion of isolated primary particles, and increased smooth surface topography. The SEM analysis reveals that the Zn-3 powder consists primarily of irregular nanocubes, with very few isolated nanoparticles, indicating that the starting material has been successfully converted into a morphology dominated by anomalous cubic structures. These changes suggest Zn acts as a mineralizer, promoting Ostwald ripening and crystal growth, while also modifying surface energy to reduce strong agglomeration. This altered morphology could significantly impact functional properties like catalytic activity and sinterability.

The analysis of Zn-2 is shown in Figure 3. The processing detected numerous particles, revealing a distribution of sizes and shapes through segmentation and centroid mapping. Histograms show the frequency distribution of particle sizes

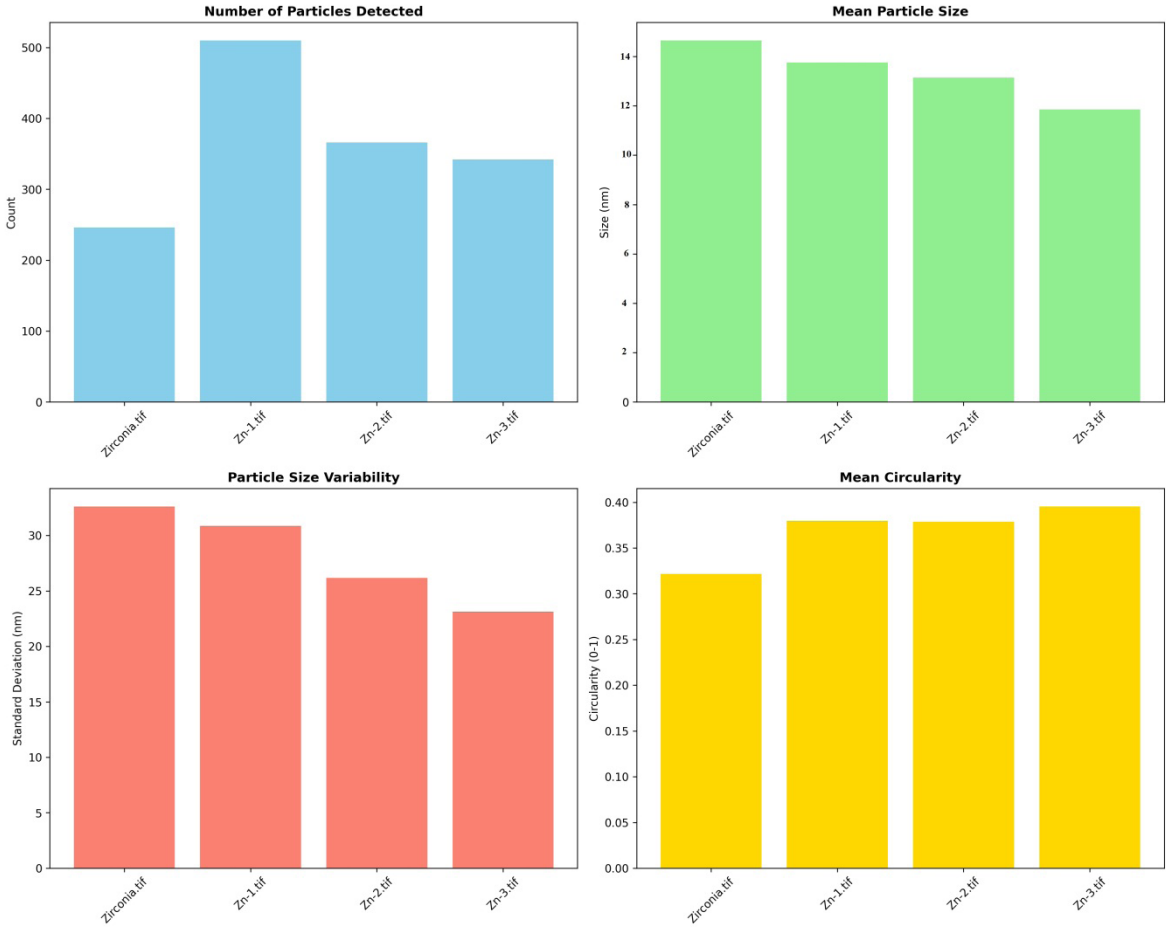
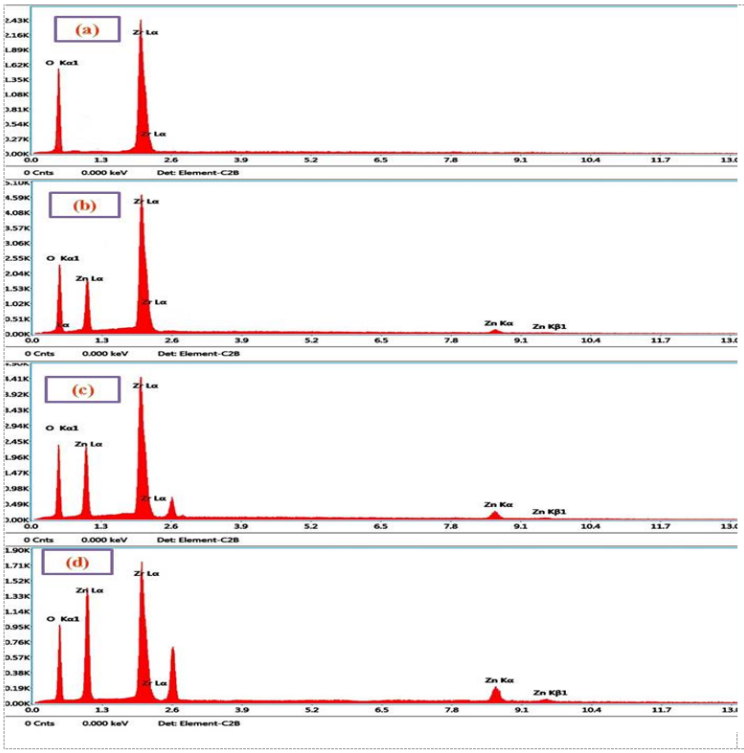


Figure 4. Comparative Analysis of pure and Zn-doped ZrO_2 nanoparticles

J Water Environ Nanotechnol, 2026, 11(SI): 113-128
10.22090/jwent.2025.2070247.1962



Sample	Elements	Weight %	Atomic %
Zn-1	Zr	52.1	17.1
	O	43.1	80.7
	Zn	4.8	2.2
Zn-2	Zr	52.2	18.5
	O	37.7	76.4
	Zn	10.1	5
Zn-3	Zr	46.1	17.3
	O	33.7	72.1
	Zn	20.2	10.6

Figure 5. EDX spectra of pure and Zn-doped ZrO_2 nanoparticles and their Elemental Composition

and circularity values, while the scatter plot explores the relationship between these parameters. The histogram reveals a relatively narrow size distribution, suggesting uniform particle growth. The circularity distribution indicates predominantly spherical morphologies, while the scatter plot shows a weak correlation between size and shape, typical of well-controlled synthesis.

The comparative analysis is shown in Figure 4. This comparative analysis reveals significant morphological differences between four samples (Zirconia, Zn-1, Zn-2, and Zn-3). The Zn-3 sample shows the smallest particle size but the largest size variability, indicating inconsistent synthesis. Zirconia exhibits the largest particles with a moderate size distribution, suggesting more controlled growth conditions. All samples show relatively low circularity values, indicating predominantly irregular, non-spherical particle shapes rather than perfect spheres. The inverse relationship between particle count and size is evident—smaller particle sizes correspond to higher particle densities. These morphological variations directly impact material properties: smaller particles typically offer higher surface area for catalytic applications, while more uniform sizes suggest better synthesis control. The irregular shapes may influence packing density and mechanical properties in final applications.

The chemical compositions and purity of the synthesized samples were analyzed using EDX, as shown in Figure 5. Figure 5(a) confirms the existence of Zr and O components, and Figure 5 (b-d) confirms the existence of Zn, Zr, and O components in the undoped and Zn-doped ZrO_2 nanoparticles. The elemental composition of Zn-doped ZrO_2 nanoparticles is listed in the table in Fig.5.

3.3 UV–Vis Analysis

Figure 6 (a) depicts the absorption spectrum of the undoped and Zn-doped ZrO_2 nanoparticles. For varied doping doses, the Uv-Vis spectra of zinc-doped zirconium oxide nanoparticles reveal an absorption edge at 380 nm, 386 nm, and 390 nm (Zn-1, Zn-2, and Zn-3). The ZrO_2 spectra revealed a minor absorption band at 235 nm and a broadband at 371 nm, both of which were at higher wavelengths than the typical bands reported for ZrO_2, generally found at about 240 nm [11]. These bands correlate to the existence of Zr species as the tetrahedral Zr^{+4} level, which is formed electrically by the charge carrier transition of the valence band O_2P electron to the conduction band Zr^{4d} (O_2 Zr^{4+}) level upon UV light stimulation [12].

The absorption edge can be observed to have migrated to the higher wavelength side following Zn doping. The redshift was detected when the Zn content in ZrO_2 increased, attributable to a change in the optical bandgap. The redshift resulted from morphological variation, and a decrease in bandgap (Eg) was attained when increased Zn content was doped in the ZrO_2 lattice.

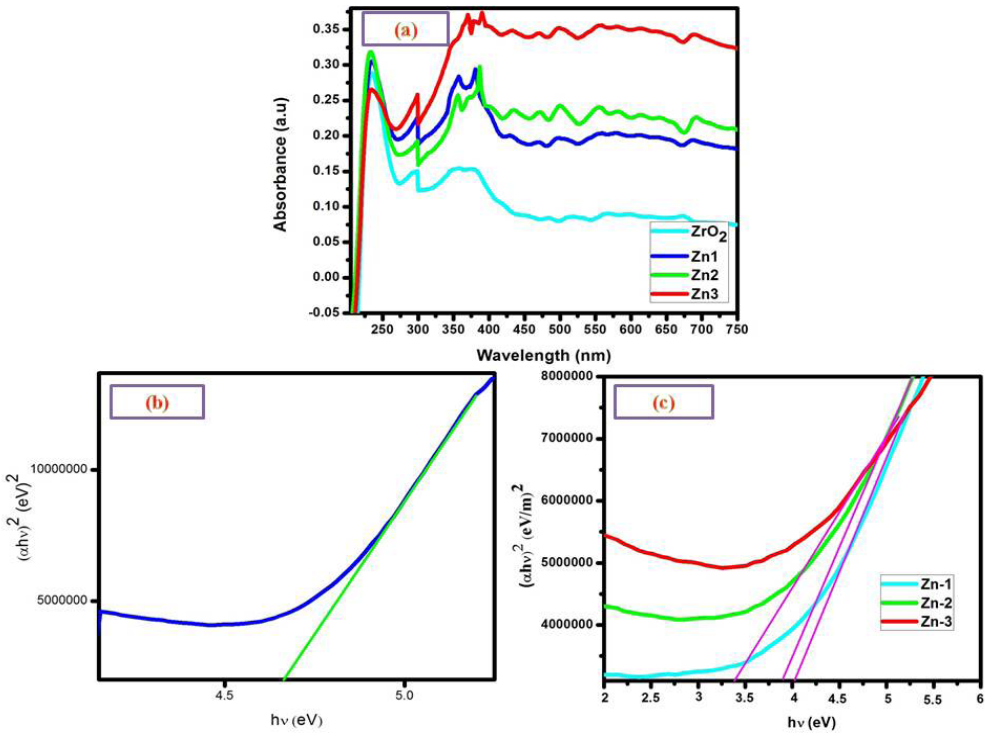


Figure 6 UV-Vis analysis of pure and Zn-doped ZrO_2 nanoparticles

To determine the bandgap of the produced nanoparticles, the Tauc relation was applied. The Tauc plot is drawn, and the energy gap is derived by extending the line to the x-axis, as shown in Figure 6(b,c).

The band gap energy of the prepared sample is calculated by using the Tauc relation,

$$(\alpha h\vartheta)^n = A\left(h\vartheta - E_g\right) \quad (7)$$

where $h\vartheta$ is the energy of a photon, E_g is the band gap energy, and A is the proportionality constant. n takes the value $1/2$ for direct allowed transitions and α is the absorption coefficient [13]. The absorption coefficient α is determined using the formula,

$$\alpha = \frac{2.303 \log\left(\frac{1}{T}\right)}{t} \quad (8)$$

Here, 'T' represents transmittance and 't' represents the thickness of the sample [14].

The energy gaps of pure and Zn-1, Zn-2, and Zn-3 doped ZrO_2 are 4.6 eV, 4.1eV, 3.9 eV, and 3.4 eV. According to optical examination, the energy gap values decreased from 4.6 eV to 3.4 eV as Zn concentration increased.

4 PHOTOLUMINESCENCE ANALYSIS

Figure 7 depicts the PL spectra of undoped and Zn-doped ZrO_2 nanoparticles with an exciting wavelength of 270 nm. The nanoparticles' PL spectra had nearly similar peak locations across the entire wavelength range. Many emission bands were found in PL spectra, including a faint ultraviolet emission at 367 nm, a weak violet emission at 419 nm, a blue emission at 485 nm, and a green emission at 542 nm. This might be because of grain boundaries, oxygen vacancies, and lattice defects in $Zn_xZr_{1-x}O_2$ NPs (x = 0.04, 0.08, and 0.12 wt percent).

When exposed to visible light, increasing the Zn^{2+} doping causes a drop in luminescence intensity due to decreased recombination of photogenerated e/h^+ couples, a faster separation rate, and a transition from the valence band to the conduction band [15,16].

5 MAGNETIC PROPERTIES

To analyze the magnetic properties of the samples at room temperature, magnetic characterization was acquired using a vibrating sample magnetometer (VSM). The magnetic parameters of pure and Zn-doped ZrO_2 nanoparticles are listed in Table 2.

The hysteresis curve, given in Figure 8, may be used to evaluate the magnetic characteristics of pure and Zn-doped

J Water Environ Nanotechnol, 2026, 11(SI): 113-128
10.22090/jwent.2025.2070247.1962

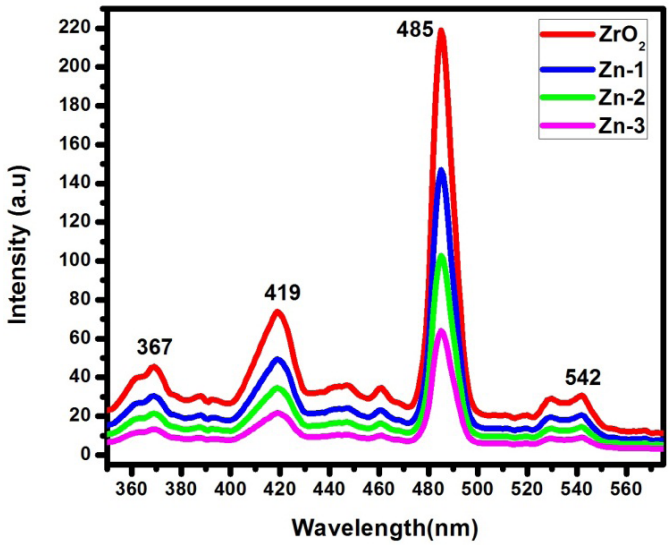


Figure 7. PL spectra of pure and Zn-doped ZrO_2 nanoparticles

Table 2 Magnetic parameters of pure and Zn-doped ZrO_2 nanoparticles

Zn concentration	Hci (Oe)	Mr (10^{-6} emu/g)	Ms (10^{-6} emu/g)	Mr/Ms
0	2535.6	53.53	586.89	0.092
Zn-1	3099.5	56.129	547.32	0.103
Zn-2	2604.3	53.624	565..10	0.095
Zn-3	1214.5	28.205	524.07	0.054

nanoparticles. When Zr^{4+} ions in ZrO_2 are replaced by Zn^{2+} ions, the magnetic properties of ZrO_2 change, namely saturation magnetization (Ms), remanent magnetization (Mr), and coercivity (Hc), with an increase in Zn^{2+} doping concentration. With increasing Zn^{2+} doping concentration, the saturation magnetization values of the doped samples increased considerably. The highest saturation magnetization value for Zn-2 is 565 emu/g, whereas the minimum value for Zn-3 is 524 emu/g.

The results in Table 3 demonstrate that saturation magnetization, coercivity, and remanence increase with increasing Zinc concentration. Hc is seen to decrease when Zn concentration rises. With 0.12wt % Zn, HC drops dramatically by more than 50%, whereas Mr drops gradually. The decrease has been linked to surface spin disorder or crystallinity fluctuations. It has been noted that H_C and Mr become very sensitive to grain size variation [17], which is consistent with the given data. At narrower ranges of crystallite size (D), H_C and Mr decreased rapidly as D increased, whereas a progressive drop was seen as D rose. This relationship is essential for Zn-doped ZrO_2. It is confirmed by the magnetic parameters listed in Table 3.

6 PHOTO-CATALYTIC ACTIVITY

The degradation of the MB dye solution under UV light irradiation was used to evaluate the photocatalytic activity of Zn-doped ZrO_2 nanoparticles. Photocatalytic degradation of MB by pure and Zn-doped ZrO_2 nanoparticles is shown in Figure 9 (a-d). The MB was a typical hazardous dye to evaluate photocatalytic activity since it had a higher absorption peak at 661nm.

The primary absorption peaks at 661nm decrease steadily over time. The decrease in the prominent absorption peak is a sign of the catalyst's minor degradation of the MB dye. After 35 minutes, the Zn-1 photocatalyst removed roughly 65 percent of the MB dye from the aqueous solution. Zn-2 and Zn-3 had 58% and 53% photocatalytic degradation efficiencies, respectively. Zn-1 (0.04 wt%) photocatalyst had

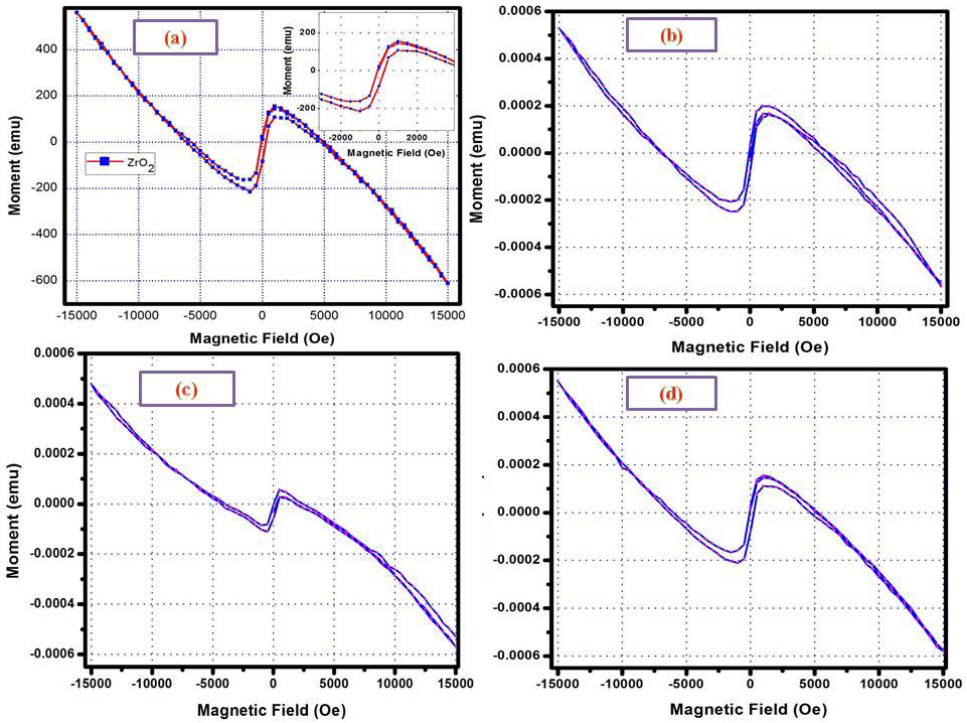


Figure 8. Hysteresis loops of pure and Zn-doped ZrO_2 nanoparticles

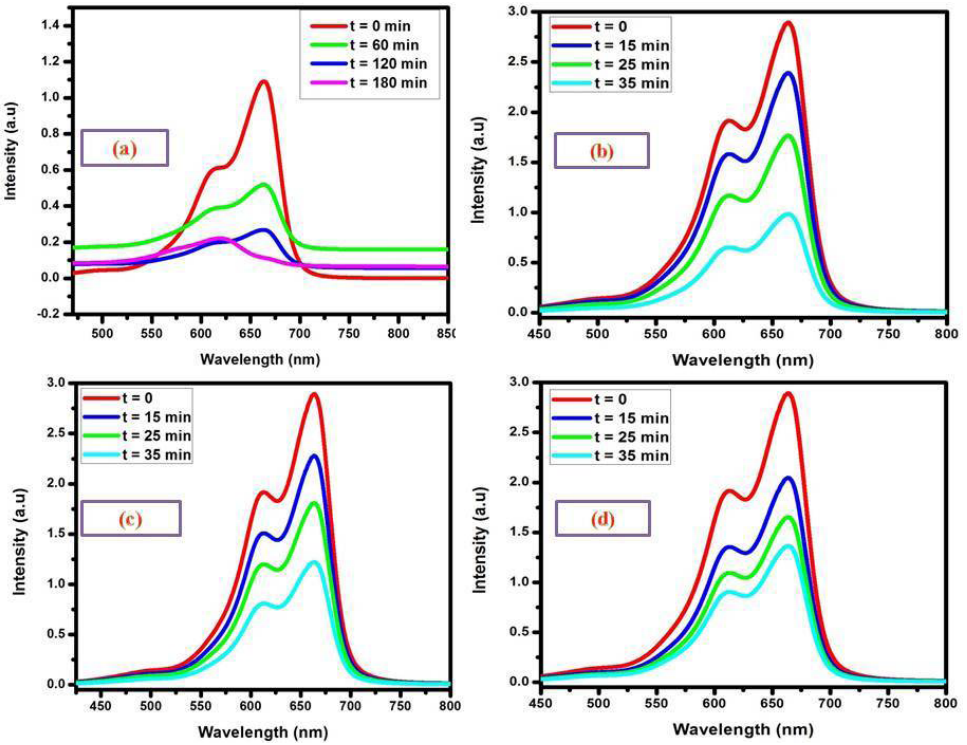


Figure 9. Photocatalytic activity of pure and Zn-doped ZrO_2 nanoparticles

J Water Environ Nanotechnol, 2026, 11(SI): 113-128
10.22090/jwent.2025.2070247.1962

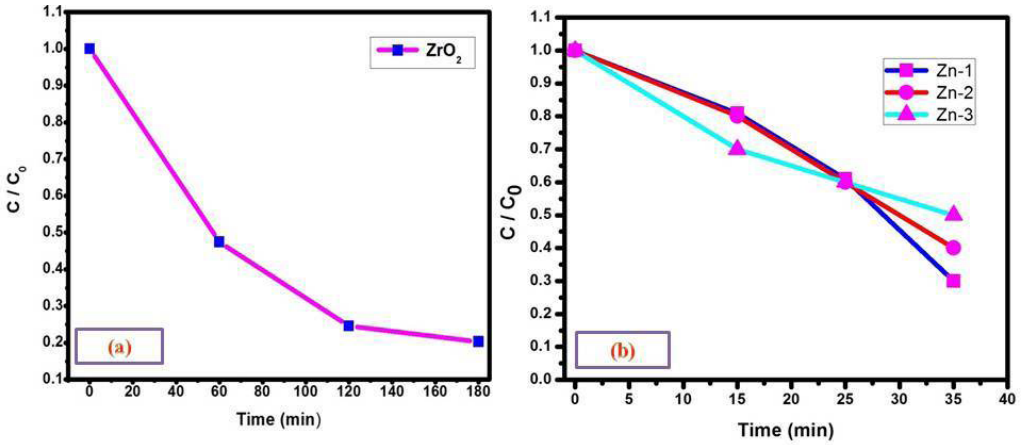


Figure 10. The normalized residual concentration of MB dye degraded by pure and Zn-doped ZrO_2 nanoparticles

Table 3. Photocatalytic degradation of Methylene Blue by undoped and Sr, Cu, Fe, and Zn doped ZrO_2

Sample	Weight %	Degradation (%)			
		t = 60 min	t = 120 min	t = 180 min	-
ZrO_2	-	53	75	80	-
Sample	Weight %	t = 5 min	t = 15 min	t = 25 min	t = 35 min
Sr-doped ZrO_2 [5]	0.04	0	39	54	65
	0.08	0	45	51	74
	0.12	0	54	77	92
Cu-doped ZrO_2 [9]	0.04	0	33	40	68
	0.08	0	34	44	78
	0.12	0	38	68	89
Fe-doped ZrO_2 [26]	0.04	0	41	45	48
	0.08	0	41	45	70
	0.12	0	34	62	93
Zn-doped ZrO_2	0.04	0	36	52	69
	0.08	0	41	58	76
	0.12	0	56	68	94

the most significant photocatalytic activity, degrading the MB dye solution by 65 percent. As a result of the findings, photocatalytic activity steadily reduced with increasing zinc levels. This might be because excess zinc acts as a recombination center and covers the active sites on the zirconium oxide surface, lowering the effectiveness of charge separation. As a result, it was critical to strike a balance between active trapping locations, which preferentially restrict electron-hole pair recombination, and less trapped regions, which primarily reduce the interfacial charge transfer separation capacity. The removal efficiency (E) of MB degradation and the normalized residual concentration of MB dye are estimated using equations 9 and 10, respectively.

$$E = \frac{C_0 - C}{C_0} \times 100 \ \ \% \tag{9}$$

where $C_0 is$ the initial concentration of dye, and C is the concentration of MB after UV irradiation.

$$\frac{C_t}{C_0} = \frac{A_t}{A_0} \tag{10}$$

where C_o and C_t are the initial and residual concentrations of MB dye. A_t and A_o are the absorbance intensity at time t and

Table 4 Anti-bacterial and Anti-fungal assessment of Zn-doped ZrO2 nanoparticles

Sample	Anti-bacterial Assessment				Antifungal assessment	
	Gram Positive		Gram Negative			
	Bacillus Subtilis (mm)	Staph aureus (mm)	Escherichia coli (mm)	Pseudomonas aeruginosa (mm)	Candida albicans (mm)	Candida parapsilosis (mm)
Amikacin	27	24	26	21	NA	NA
Zn-1	21	18	16	15	19	17
Zn-2	18	21	18	20	20	16
Zn-3	15	23	19	16	14	16
Nystatin	NA	NA	NA	NA	27	20

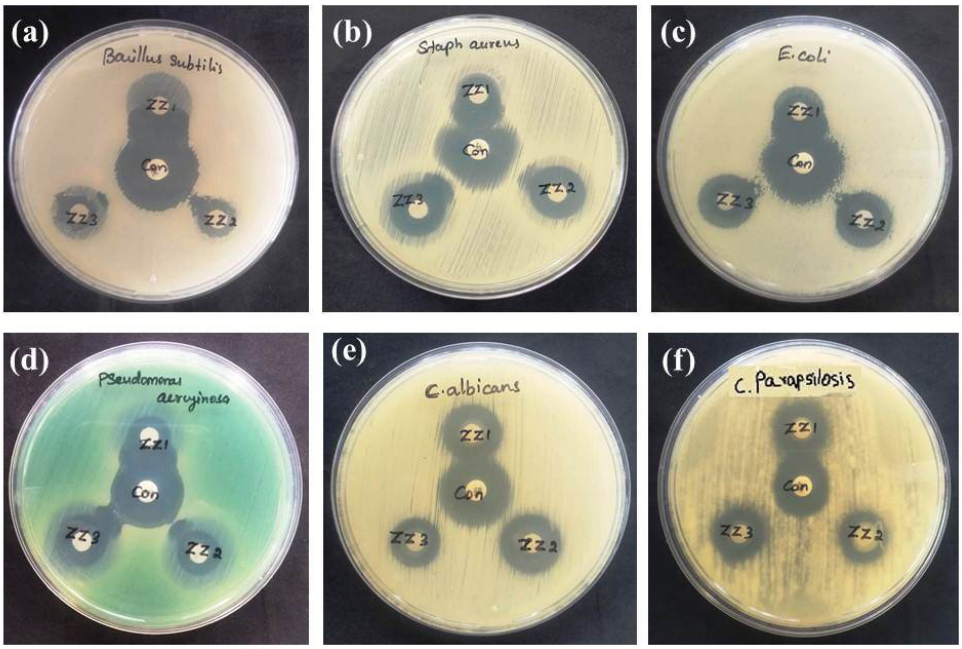


Figure 11. Anti-bacterial and Anti-fungal effect of Zn-doped ZrO_2 nanoparticles

at time t = 0 obtained from the UV-absorbance spectrum. The normalized residual concentration of MB dye degraded by pure and Zn-doped ZrO_2 nanoparticles is shown in Figure 10 (a,b). The percentage of Methylene Blue degradation by undoped and Sr, Cu, Fe, and Zn doped ZrO_2 is listed in Table 3.

7 ANTI-BACTERIAL AND ANTI-FUNGAL MICROBIAL ASSESSMENT

The disc diffusion method was used to test the antimicrobial activities of pure and Zn-doped ZrO_2 samples against gram-positive bacteria (*Bacillus Subtilis*, *Staphylococcus aureus*), gram-negative bacteria (*Escherichia coli*, *Pseudomonas aeruginosa*), and two fungi (*Candida albicans*, *Candida parapsilosis*) strains. Anti-bacterial and Anti-fungal assessment of Zn-doped ZrO_2 nanoparticles is shown in Table 4.

Figure 11 (a-d) depicts the anti-bacterial inhibition zones of Zn-doped ZrO_2 samples with varying Zn concentrations. It is noted that the maximum inhibition zone of the pure ZrO_2 exhibits around 28mm against Gram-positive bacteria, namely *Staphylococcus aureus,* compared to other bacterial and fungal strains. Also, Zn-doped ZrO_2 nanoparticles, the inhibition zone was found to be around 23 mm in Gram-positive bacteria such as *Staphylococcus aureus*. For other bacterial strains, when the concentration of Zinc increases, the inhibition zone is reduced. It was concluded that the zinc-doped zirconium oxide nanoparticles act as a good anti-bacterial agent.

J Water Environ Nanotechnol, 2026, 11(SI): 113-128
10.22090/jwent.2025.2070247.1962

Figure 11 (e,f) depicts the anti-fungal inhibition zones of Zn-doped ZrO_2 samples with varying Zn concentrations. As shown in Figure 11 (e,f), the antifungal activity of the pure and doped materials was tested against two fungal strains (*Candida albicans* and *Candida parapsilosis*). The Zn-2 sample is more active against Candida albicans compared to other fungal strains, and the inhibition zone measured around 20 mm. The inhibition zone of the samples is compared with the control amikacin for the bacterial strain and nystatin for the fungal strain. Thus, the zinc-doped ZrO_2 nanoparticles possess a moderate anti-microbial effect.

7 CONCLUSION

Zn-doped ZrO_2 nanoparticles were successfully prepared by the co-precipitation method. Their Structural, optical, magnetic, photocatalytic, and antimicrobial properties were investigated under various characterization techniques. XRD analysis indicated that crystallite size increases with dopant concentration without altering the original tetragonal phase. SEM morphology showed the formation of nanocubes for Zn-3 nanoparticles. The integration of YOLOv8 and ConvNeXt significantly advances SEM image analysis by enabling automated, high-precision segmentation and morphological quantification of nanoparticles. This deep learning approach provides reproducible, bias-free measurements of size, shape, and agglomeration and surface topography. UV-VIS research reveals a redshift with increasing Zn content in ZrO2, which is related to a change in the optical band gap, ranging from 4.6 eV to 3.4 eV. The PL study revealed that increasing the Zn^{2+} doping causes a reduction in luminescence intensity. From the photocatalytic results, the photocatalytic activity was found to decrease gradually with a large amount of zinc content, and 65% of methylene blue dye degradation within 35 minutes was observed for low dopant concentration. Zinc-doped ZrO_2 nanoparticles act as a good anti–microbial agent.

Conflict of Interest
The authors declare that they have no known competing financial interests or personal relationships that could have appeared to influence the work reported in this paper.

Funding
This study was not supported by any funding.

Author contributions:
Jeba R. performed the synthesis and material preparation. Radhika S. proposed the concept and performed the experimental design. Ascar Davix. X assisted in the analysis of data and manuscript preparation.

AI Statement
The authors confirm that no AI tools or services were used during the preparation of this work.

REFERENCES

1. Zalnezhad, E, Hamouda, AMS, Jaworski, J, & Do Kim, Y 2016, 'From zirconium nanograins to zirconia nanoneedles'. Scientific reports, vol.6, no.33282.
2. Jeba, R, Radhika, S, Padma,CM & Ascar Davix, X, 2021, 'Structural, Optical, Thermal, Magnetic Properties of Zirconia Nanorods and their Photocatalytic and Antimicrobial Properties', Journal of Water and Environmental Nanotechnology, vol.6, no.3, pp.252-264.
3. Jeba, R, Radhika, S, Padma,CM & Ascar Davix, X, 2022, 'Antimicrobial and photocatalytic activities of strontium doped zirconium oxide nanoparticles', Materials Letters, vol. 311,no. 131559.
4. Jeba, R, Radhika, S, Padma,CM & Ascar Davix X, 2022, 'Synthesis and characterization of zirconia nanorods as a photo catalyst for the degradation of methylene blue dye', Nanosystems: Physics, Chemistry, Maths, vol.13 (1), pp.78–86.
5. Jeba, R, Radhika, S, Padma,CM & Ascar Davix, X, 2022, 'Strontium doped zirconia for enhanced anti-microbial activity', Materials Today: Proceedings,vol.58,pp.927-931.
6. Qu, X, Alvarez, PJJ & Li, Q 2013, 'Applications of nanotechnology in water and wastewater treatment', Water Research, vol.47, pp.3931–3946.
7. Abdullah Goktas, Sait Modanlı, Ahmet Tumbul, Ahmet Kilic, 2022, 'Facile synthesis and characterization of ZnO, ZnO:Co, and ZnO/ZnO:Co nano rod-like homojunction thin films: Role of crystallite/grain size and microstrain in photocatalytic performance', Journal of Alloys and Compounds, Volume 893. no. 162334.
8. P. Joshi, S. Chakraborti, P. Chakrabarti, D. Haranath, V. Shanker, Z. A. Ansari, S. P. Singh, and V. Gupta, J. Nanosci. Nanotechnol. 9, 6427 (2009).
9. Jeba, R, Radhika, S, Padma,CM & Ascar Davix, X, 2022, 'The influence of Cu doped ZrO2 catalyst for the modification of the rate of a photoreaction and forming microorganism resistance', Journal of Water and Environmental Nanotechnology, vol.7, no.4, pp.351-362.
10. Raja,K, Ramesh,P & Geetha,D 2014, 'Structural, FTIR and photoluminescence studies of Fe doped ZnO nanopowder by co-precipitation method', Spectrochimica Acta Part A, vol. 131, pp.183–188.
11. Kanade,KG, Baeg,JO, Apte,SK, Prakash,TL & Kale,BB 2008, 'Synthesis and characterization of nanocrystallined zirconia by hydrothermal method', Materials Research Bulletin, vol. 43, no. 3, pp. 723–729.
12. Sreethawong,T, Ngamsinlapasathian,S & Yoshikawa,S 2013, 'Synthesis of crystalline mesoporous-assembled ZrO2 nanoparticles via a facile surfactant-aided sol–gel process and their photocatalytic dye degradation activity', Chemical Engineering Journal, vol. 228, pp. 256–262.
13. Radhika,S, Padma,CM,.Ramalingom,S &.ChithambaraThanu T 2013, 'Growth, optical, thermal, mechanical and dielectric studies of potassium sulphate crystals doped with urea', Archives of Physics Research, vol.4, no.1, pp.49-59.
14. Sadeghzadeh-Attar, A 2018, 'Efficient photocatalytic degradation of methylene blue dye by SnO2 nanotubes synthesized at different calcination temperatures', Solar Energy Materials and Solar Cells, vol.183, pp. 16-24.
15. Singh,RK, Narayan,A, Prasad,K, Yadav,RS, Pandey,AC, Singh,AK, Verma,L & Verma, RK 2012, 'Thermal, structural,

magnetic and photoluminescence studies on cobalt ferrite nanoparticles obtained by citrate precursor method', Journal of Thermal Analysis and. Calorimetry, no.110, pp. 573–580.
16. Sundararajan, M, Sailaja, V, John Kennedy, L & Judith Vijaya,J 2017, 'Photocatalytic degradation of rhodamine b under visible light using nanostructured zinc doped cobalt ferrite: kinetics and mechanism', Ceramics International, vol. 43,no.1,pp.540–548.
17. Vollath, D 2008, 'Nanomaterials: an introduction to synthesis, properties and applications', WILEY-VCH Verlag GmbH & Co.KGaA, Germany.
18. Aman K. Chitoria, Arshid Mir, M.A. Shah, A review of ZrO2 nanoparticles applications and recent advancements, Ceramics International, Volume 49, Issue 20, Pages 32343-32358.
19. E. Indrajith Naik, H.S. Bhojya Naik, R. Viswanath, B.R. Kirthan, M.C. Prabhakara, Effect of zirconium doping on the structural, optical, electrochemical and antibacterial properties of ZnO nanoparticles prepared by sol-gel method, Chemical Data Collections, Volume 29, October 2020, 100505.
20. Winczewski, J., Arriaga-Dávila, J., Maestre, D., Herrera-Zaldívar, M., Gardeniers, H. and Susarrey-Arce, A. (2024), Additive Manufacturing of Zn-Doped ZrO2 Architectures. Adv. Eng. Mater., 26: 2400187. https://doi.org/10.1002/adem.202400187.
21. Masakazu Gesho, Wattana Chaisoontornyotin, Omar Elkhatib, Lamia Goual, "Auto-segmentation technique for SEM images using machine learning: Asphaltene deposition case study" Ultramicroscopy, 217 (2020) 113074.
22. Yoichi Takagishi , Yoshiki Hayashi , Takayuki Tsubota , Tatsuya Yamaue, "Modelling of SiOx electrode degradation based on latent variables from 2D-SEM images" Journal of Energy Storage, 105 (2025) 114621.
23. Tahereh Rohani Bastami, Mohammad H. Entezari, High stable suspension of magnetite nanoparticles in ethanol by using sono-synthesized nanomagnetite in polyol medium, Materials Research Bulletin, Volume 48, Issue 9, September 2013, Pages 3149-3156.
24. Janbibi Dorazehi, Masumeh Farrokhi, Tahereh Rohani Bastami, Zahra Meshkat , Vahid Mahmoudi, Hamid Tanzadehpanah, Hesamaddyn Babaei, Exploration of the antiviral and antibacterial efficacy of hydrozincite/graphene oxide nanocomposites: Molecular docking and in vitro investigations, Journal of Environmental Chemical Engineering, Volume 13, Issue 5, October 2025, 118940.
25. Marjan Tanzifi, A Review on Application of Noble Metal-Free Materials/ZrO2 Nano-photocatalysts for Removal of Organic Pollutants and Heavy Metals, Journal of Water and Environmental Nanotechnology, Volume 9, Issue 3, 2024, Pages 263-286.
26. Jeba, R, Radhika, S, Ascar Davix, X, Juliet Brintha,CS, The Impact of Fe-doped Nano Zirconia for the Reformation of the Photoreaction Rate and Materializing Microorganism Resistance, Journal of Water and Environmental Nanotechnology, Volume 10, Issue 1, 2025, Pages 47-60.